# Super ductile metallic glasses for energy-saving solid-state processing

T. Barriere[♭*], F. Bernard[‡], X. Gabrion[♭], S. Carbillet[♭], S. Holopainen[†*], N. Niang[♭], Jean-Mark Pelletier[♯], Wei-Hua Wang[♮]

[♭] *Univ. Bourgogne Franche-Comté, FEMTO-ST Institute, CNRS/UFC/ENSMM/UTBM, Department of Applied Mechanics, 25000 BESANÇON-FR, France.*

[‡] *Univ. Bourgogne, ICB - UMR 6303 CNRS, Marey Institute - House of Metallurgy, 221000 Dijon-FR, France.*

[†] *Tampere University, Department of Civil Engineering, FI-33014 Tampere, Finland.*

[♯] *Univ. de Lyon, CNRS, INSA-Lyon, MATEIS UMR5510, F-69621 France.*

[♮] *The Institute of Physics, Chinese Academy of Sciences. Beijing, China.*

**Abstract**

Energy-efficient materials are key to combating the high energy costs and climate change. The manufacturing temperatures of industrially important Zr-based bulk metallic glasses (BMGs) relative to steels are low, and exist between the liquidus temperature $T_l$ (∼850 °C) and glass transition temperature $T_g$ (∼400 °C). However, these materials show limited plastic deformability (ductility) at room temperature (strains typically less than 3 %); moreover they soften but exhibit limited ductility at high processing temperatures. Their low ductility should be improved because it impedes fatigue resistance and machinability, such as via cold (plastic) forming. In this study, chemical composition changes, which reduced $T_g$, resulted in remarkably ductile BMGs with extreme deformations of over 70 % under compression, thereby enabling their energy-efficient processing at low temperatures. In contrast to previously reported conclusions on the high GFA and deformation-induced nanocrystallization being the precursors to ductility, formation of a low amount of meso-crystallites within the glassy material during cooling efficiently hindered the propagation of shear bands (SBs) and microcracks under loading, thus increasing significantly ductility. This characteristic, in addition to optimal chemical composition, played an important role in improving the ability of BMGs to undergo solid-state processing at low temperatures and increased deformation rates.

*Keywords:* BMGs, Softening & hardening, Shear banding, Chemical composition, Crystallization

## 1. Introduction

The advantageous properties of BMGs are directly due to their non-crystalline structure that lacks defects, such as dislocations, which are present in conventional crystalline metals and alloys. BMGs have an extremely high yield strength (∼1.8 GPa), that is, a high strength-to-weight ratio, high elastic deformability (2 - 5 %), high thermal stability, and strong corrosion resistance [1–4]. Therefore they are suitable functional materials for high-tech electronic devices, aerospace applications, nuclear reactors, automotive, sporting goods, and surface coatings (cold spraying) [5, 6]. The global market size of glassy metals was USD 1.49 billion in 2019, and the highest growth in product consumption occurred in the electronics sector [7].

However, the lack of ductility, that is, low plastic deformability, fracture toughness, and damage tolerance (the product of yield strength and fracture toughness [8]) especially in tension and fatigue loadings, impedes their machinability and practical use [3, 4, 9–14]. Improving the ductility fairly below $T_g$ ($T/T_g < 0.5$) would make BMGs suitable for solid-state processing (which processing further improves ductility [15, 16]), such as mechanical alloying and cold working (forming, rolling, imprinting) [6, 17, 18]. Additionally, improving the

*Correspondence to e-mails: sami.holopainen@tuni.fi, thierry.barriere@univ-fcomte.fr

low-temperature ductility also enhances ductility at high processing temperatures by reducing the formation of localized SBs [8, 11, 15].

The ductility of BMGs can be improved by various methods such as (a) ion irradiation [6], (b) cryogenic thermal cycling that affects rejuvenation [19, 20], (c) structural modification (e.g., cold rolling and surface imprinting) [9, 16], (d) deformation(stress)-induced nanocrystallization (under compression) [16, 21, 22], (e) hydrogen microalloying [23], and (f) rejuvenation under triaxial compression at room temperature (RT; about 20°C) [12]. However, thermal cycling methods (b) increase energy consumption and often reduce the strength of BMGs [23], whereas pre-deformation methods (c,d,f) may distort their shape and weaken glassy structure, thereby restricting their application [8, 19]. Moreover, the increase in ductility achieved by these methods (a) - (f) has been limited; ultimate macroscopic strains lower than 20 % have been realized [6, 16, 19, 23–25]. Micro-alloying, that is, varying the chemical composition, is more efficient method for improving ductility [10, 26, 27], and it was used in this research.

In contrast to previous research on the restricted deformability of BMGs [4, 18, 28], the optimal chemical compositions $Zr_{65}Cu_{15}Ni_{10}Al_{10}$, $Zr_{52.5}Cu_{17.8}Ni_{14.5}Al_{10}Ti_5$, and $Zr_{40}Ti_{25}Cu_8Be_{27}$ resulted in the BMGs exhibiting compressive ultimate strains ($\epsilon_u$) of over 70 % at RT and strain rates of almost 0.04 1/s. This extremely high ductility (malleability), even over their granulate-based composites (BMGCs), was due to the sufficient content of nanoscopic embedded crystallized particles and their microscopic clusters within the glassy material, which were formed during sufficiently slow cooling. That is, the statement *slower cooling reduces plasticity* [12] is not completely valid. Instead, the extremely high ductility and plasticity achieved with a low crystallization offers several possibilities for accommodating working processes at lowered temperatures, even near RT. The effects of chemical composition changes and included crystallites on mesoscopic structural changes and macroscopic deformation behavior (softening and hardening) at different loading rates and temperatures were investigated in the present study.

## 2. Results and discussion

The following Zr-based BMGs (at%) were compared: (i) $Zr_{57}Cu_{20}Ni_8Al_{10}Ti_5$ [24], (ii) $Zr_{48}Cu_{45}Al_7$ [29], (iii) $Zr_{65}Cu_{18}Ni_7Al_{10}$ [30], (iv) $Zr_{65}Cu_{15}Ni_{10}Al_{10}$, (v) $Zr_{52.5}Cu_{17.8}Ni_{14.5}Al_{10}Ti_5$, and (vi) $Zr_{40}Ti_{25}Cu_8Be_{27}$. The results for the compositions (i) - (iii) were taken from the literature, and the compositions (iv) - (vi) were tested in our laboratory, see *Methods*. As shown in Table 1 and Fig. 1(a), compositions (i) - (iii), although have been previously reported to be ductile state-of-the-art compositions [24, 29, 30], were actually not much ductile (super ductile), because, due to a high Cu content or low Ni/Al content ratios (without enriching with Ti or Be), they exhibited limited plastic deformability ($\epsilon_u \sim 0.1$) followed by rapid fracture when the plastic flow shows extreme localization within SBs [12, 15]. Composition (i) showed strain-hardening, that is, the increase of flow stress with plastic strain [8] and the second yield strength $\sigma_c$ that was greater than the (first) yield strength $\sigma_y$ ($\sigma_y < \sigma_c$). Compositions (ii) with the highest Cu content and (iii) ~~with the highest Cu content~~ with a low Ni/Al content ratio showed pure softening, i.e., $\sigma_c$ values that were lower than $\sigma_y$ ($\sigma_y > \sigma_c$). A comparison between the compositions (iii) and (iv) shows the sensitive dependence on Cu/Ni relationship and the loading rates applied, Fig. 1(a-b). A rapid transition from stable to unstable deformation making the material brittle has been reported to be due to multiple concentrated SBs (with increasing deformation rate) [30, 31] and subsequent fracture surfaces (a local increase in temperature) where SB patterns (straight slip planes) were different from the typical vein-like patterns improving ductility [22, 30, 31].

Compositions (iv) - (vi), which exhibited the highest ductility among the samples and had a low Cu content and increased Zr/Ti/Be contents, showed hardening followed by softening and yet re-hardening at strain rates close to $\dot{\epsilon} = 0.04$ 1/s. Similar extreme ductility for the composition (iv) have previously been evidenced in Qiu et al. [22], but at low strain rate $\dot{\epsilon} = 0.0001$ 1/s. The hardening-softening was characterized by a reduced stress development that occurred in two stages: first, a reduced stress development ($\sigma_y < \sigma_c$) followed by a second, intense stress drop, as shown in Figs. 1(b-f) (the two extremes of the test results are displayed) and 2(a). Fig. 2(c) reveals that the ratio $\sigma_y/\sigma_c$ increases with increasing strain rate $\dot{\epsilon}$, which observation is also evident from previous works [31, 36], although at low strain rates, $\dot{\epsilon} < 5E-5$ 1/s. That is, the higher $\dot{\epsilon}$, the higher the ratio $\sigma_y/\sigma_c$ and the lower the ductility. Moreover, a reduction in the stresses $\sigma_y$ and $\sigma_c$ with increasing strain rates can be observed. This characteristic contrasts that of crystalline metals and glassy polymers, whose yield stress increases with strain rate [30, 31, 39, 40]. The influence of the compositions on the yield strength $\sigma_y$ and yield strain $\epsilon_y$ is further illustrated in Fig. 2(d), where the

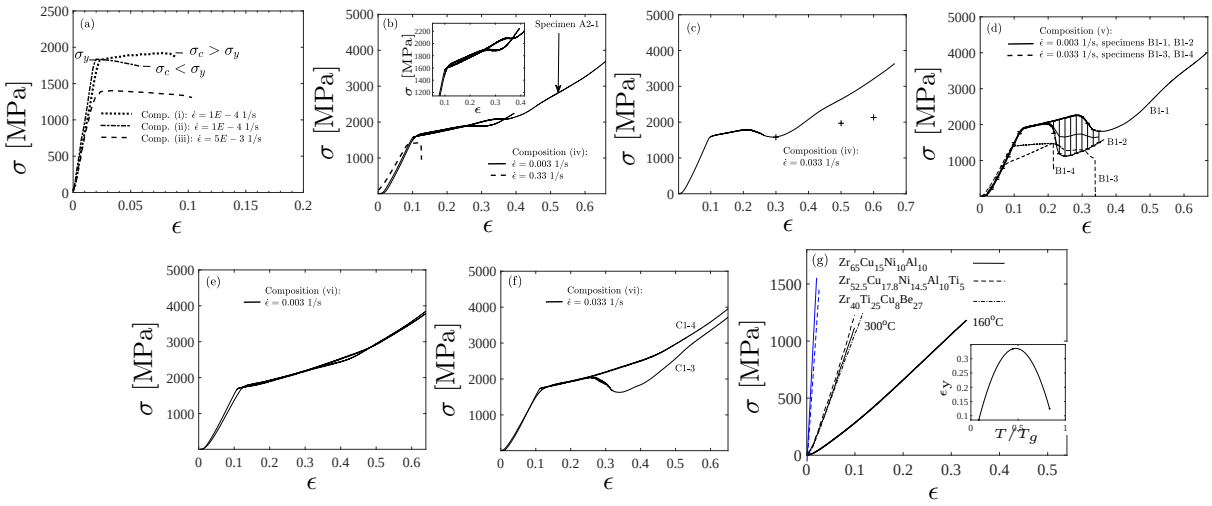


Figure 1: Measured stress-strain ($\sigma-\epsilon$) responses at RT for different state-of-the-art compositions (sufficiently accurate copies for the main characteristics) taken from [24, 29, 30] (a). Responses of composition (iv) (b). The inset shows serrated flow prior to hardening. Responses of composition (iv) at $\dot{\epsilon} = 0.033$ 1/s (c). The markers '+' denote the true stress, cf. *Methods*. Responses of composition (v) at $\dot{\epsilon} = 0.0033$ 1/s (solid) and $\dot{\epsilon} = 0.033$ 1/s (dashed) (d). Averaged data with error bars (for 0.003 1/s) are shown. Responses of composition (vi) at $\dot{\epsilon} = 0.0033$ 1/s and $\dot{\epsilon} = 0.033$ 1/s (e-f). Responses for compositions (iv) - (vi) at 300°C when $\dot{\epsilon} = 0.0033$ 1/s (g). The response of composition (iv) at 160°C is also shown, with the inset showing the yield strain limit as a function of temperature. Benchmarks for $Zr_{64}Cu_{16}Ni_{10}Al_{10}$ ($\dot{\epsilon} = 0.0002$ 1/s) at 300°C (solid blue) and 150°C (dashed blue) [32].

two clusters are observed. Compositions (v) - (vi) in the second cluster are most ductile (incl. Ti and/or Be; the largest products $\sigma_y\epsilon_y$ and $\sigma_y\epsilon_y\dot{\epsilon}$, cf. Table 1). When replacing Ti and/or Be essentially by Zr (composition (iv)), the ductility is yet high compared to the compositions (i) - (iii) (high Cu-content or low Ni/Al relationship). These results are also reflected in the second yield strengths $\sigma_c$ shown in Fig. 2(e), although the deviation is larger. When the strain rate was sufficiently high ($\dot{\epsilon} = 0.33$ 1/s and $\dot{\epsilon} = 0.033$ 1/s for compositions (iv) and (v), respectively), also the most ductile BMGs exhibited rapid fracture, Fig. 1(b,d). These results indicated that the strain rate controlled the deformation mode transition from stable shear-dominated sliding towards unstable cracking-dominated fracture [30]. A large deviation in the test results was observed for composition (v), in which some Zr was substituted with Ni and Al; the largest error bars shown in Fig. 1(d).

The following observations (A-C) were also made based on the experimental results shown in Figs. 1(b-f), 2(a-b), and 3. (A) During the first hardening of composition (iv), inhomogeneous but a regular set of multiple thin, 1 - 10 nm thick SBs (a magnitude thinner compared to crystalline metals [15]) representing slip planes with a mutual distance of approximately 5 $\mu$m [30, 35, 36] was formed as illustrated in Fig. 2(a). From atomic to nanoscopic level, the hardening-softening described above was presumed to be directly related to the two-phase disordering of the material within SBs: local cluster of atoms/nanoparticles undergoes two-

Table 1: Comparison of the yield strengths $\sigma_y$ and $\sigma_c$, and the corresponding yield strains $\epsilon_y$ and $\epsilon_c$ of Zr-based BMGs (mean values). The ultimate strains $\epsilon_u$ and corresponding strain rates are mentioned.

| Monotonic tests | | | | | | |
|---|---|---|---|---|---|---|
| Material's ID | $\sigma_y$ (MPa) | $\sigma_c$ (MPa) | $\epsilon_y$ (-) | $\epsilon_c$ (-) | $\dot{\epsilon}$ ($s^{-1}$) | $\epsilon_u$(−) |
| $Zr_{57}Cu_{20}Ni_8Al_{10}Ti_5$ (i) ..... | 1,810 | 1,850 | 0.02 | 0.09 | 0.0001 | 0.09 |
| $Zr_{48}Cu_{45}Al_7$ (ii) ..... | 1,820 | 1,720 | 0.02 | 0.04 | 0.0001 | 0.07 |
| $Zr_{65}Cu_{18}Ni_7Al_{10}$ (iii) ..... | 1,390 | 1,340 | 0.02 | 0.12 | 0.005 | 0.11 |
| $Zr_{65}Cu_{15}Ni_{10}Al_{10}$ (iv) ..... | 1,590 | 1,950 | 0.11 | 0.31 | 0.003 | 0.68 |
| $Zr_{52.5}Cu_{17.8}Ni_{14.5}Al_{10}Ti_5$ (v) .. | 1,840 | 2160 | 0.12 | 0.24 | 0.003 | 0.67 |
| $Zr_{40}Ti_{25}Cu_8Be_{27}$ (vi) ..... | 1,730 | - | 0.12 | - | 0.003 | 0.67 |

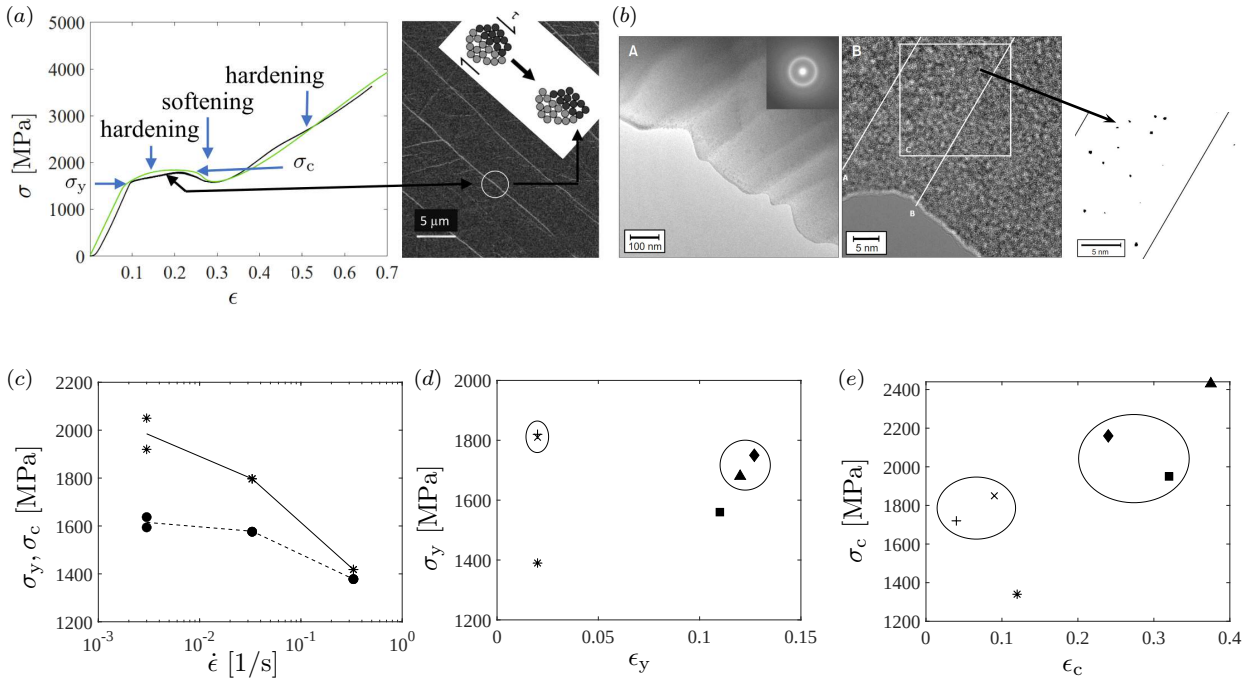


Figure 2: Stress vs. strain and a SEM image for the illustration of thick slip planes (white) in the composition (iv) during hardening (a). Schematics of atomistic disordering in STZs (by Argon, 1979) and the shear resistance $'\tau'$ along the slip planes [15]. SBs (white lines and shadows) in the vicinity of a microcrack's tip (grey region in bottom left) in $Zr_{52.5}Cu_{20}Ni_8Al_{10}Ti_{17.9}$ observed by TEM during hardening [15, 41] (b). The SBs have been identified by an increased degree of the free volume (white regions) accumulated preferentially between the boundaries of the SBs (the two lines shown in (B)). Measured yield strengths $\sigma_y$ (dashed curve) and $\sigma_c$ (solid) vs. strain rate for composition (iv) at RT (c). Charts representing the yield strengths vs. corresponding yield strains for different chemical compositions: (i) (marker x), (ii) (marker +), (iii) (marker $*$), (iv) (marker ■), (v) (marker ♦), and (vi) (marker ▲) (d-e). Data represent mean values, also shown in the table 1. Two observed clusters are highlighted by ellipses.

phase rearrangement to form a higher free-volume and energy configuration [31], that is, slow disordering followed by a rapid one affecting dilatation through additional free volume within SBs [6, 12, 21, 33, 34]. The formation of SBs per se is known from previous literature [15, 17]: coalescence of voids (free volume) which accumulated preferentially between the boundaries of emerging SBs, cf. Fig. 2(b). (B) This formation of SBs and slip planes during the hardening have been reported to affect the serrated flow that is typical of BMGs [15, 30, 31, 37] as shown in Fig. 1(b). Fig. 3 shows micrographs at the beginning of softening when the serrated flow was largest. Two onsets for emerging SBs and their slip planes can be observed: (1) high-stressed edges of cavities or protrusions (Fig. 3(a-b,d-e)) and (2) high-stressed flat surfaces between protrusions (Figs. 3(c,f)), which can deliver microcracks during re-hardening. The amplitude of the serrated curve decreased or even disappeared during softening and with increasing strain rate [30, 31] because the progress of SBs and slip planes ceased, in contrast to that in steels [17, 35, 36]. It is noteworthy that the Ti/Be-based compositions (v) and (vi) did not show serrated flow, Fig. 1(d-f). Based on the SEM fractographs conducted this desired stable property is probably due to the capability of the Ti/Be-based mixture to form vein-like patterns and rippled zones of SBs instead of regular SBs and slip planes [31, 36, 38].

After the softening stage, the scenario featuring the SBs rapidly change, and yet more dissipation energy was required for secondary SBs (SB diffusion and delocalization of the plastic flow in SBs [12]) and deformation. Consequently, the macroscopic responses showed re-hardening and extreme plastic deformation as shown in Fig. 1(b-f). ~~(b) When the strain rate was sufficiently high ($\dot{\epsilon} = 0.33$ 1/s and $\dot{\epsilon} = 0.033$ 1/s for compositions (iv) and (v), respectively), also the most ductile BMGs exhibited rapid fracture, Fig. 1(b,d). These results indicated that the strain rate controlled the deformation mode transition from stable shear-dominated sliding towards unstable cracking-dominated fracture [30]. (c) A large deviation in the test results was observed for composition (v), in which some Zr was substituted with Ni and Al; the largest error~~

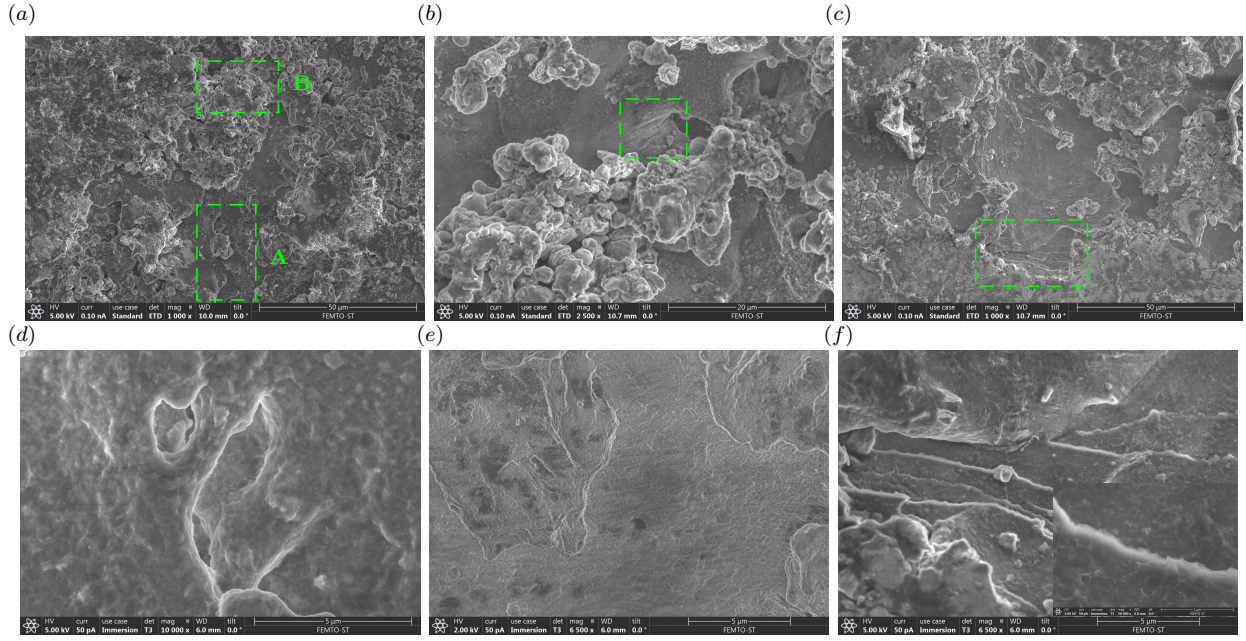


Figure 3: Scanning electron microscopy (SEM) images acquired at the beginning of softening of a monotonic compression test ($V = 0.1$ mm/s, RT, $Zr_{65}Cu_{15}Ni_{10}Al_{10}$) showing onsets of SBs (a-b) and slip planes (c) for microcracks (dashed frames). Detailed SEM images (d-e) showing the onsets of SBs (white curves) in (a) (inside the frames A and B, respectively). The emerging slip planes (surfaces) (f) in accordance with (c) (inside the dashed frame). The inset shows a zoom of a slip surface.

~~bars shown in Fig. 1(d).~~ (C) A comparison of compositions (iv) - (vi) revealed that the re-hardening that followed softening was not sensitive to the investigated chemical compositions, that is, the increase of stress with plastic strain shown in Fig. 1(b-f) were similar.

To this end, the responses in Fig. 1(g) reveal that the compositions softened at 160°C and 300°C, and exhibited linear but essentially irreversible (plastic) macroscopic deformation behavior. The yield strength limit was reduced by one-third compared with the results obtained at RT (before softening). However, the ductility (the products $\sigma\epsilon$ and $\sigma\epsilon\dot{\epsilon}$) was much greater than observed in previous state-of-the-art results [32]. Based on the samples for the three temperatures (RT, 160°C, 300°C), the highest yield strain limit was achieved at $T/T_g = 0.4$ (~130°C).

~~Fig. 2(e) reveals that the ratio $\sigma_y/\sigma_c$ reduces with increasing strain rate $\dot{\epsilon}$, which observation is also evident from previous works [31, 36], although at low strain rates, $\dot{\epsilon} < 5E-5$ 1/s. That is, the lower $\dot{\epsilon}$, the lower the ratio $\sigma_y/\sigma_c$ and the higher the ductility. Moreover, a small reduction in the stresses $\sigma_y$ and $\sigma_c$ with increasing strain rates can be observed. This characteristic contrasts that of crystalline metals and glassy polymers, whose yield stress increases with strain rate [30, 31, 39, 40]. The influence of the compositions on the yield strength $\sigma_y$ and yield strain $\epsilon_y$ is further illustrated in Fig. 2(d), where the two clusters are observed. Compositions (v) - (vi) in the second cluster are most ductile (incl. Ti and/or Be; the largest products $\sigma_y\epsilon_y$ and $\sigma_y\epsilon_y\dot{\epsilon}$, cf. Table 1). When replacing Ti and/or Be essentially by Zr (composition (iv)), the ductility is yet high compared to the compositions (i) - (iii) (high Cu-content or low Ni/Al relationship). These results are also reflected in the second yield strengths $\sigma_c$ shown in Fig. 2(c), although the deviation is larger.~~

In summary, when investigating the ultimate strains $\epsilon_u$ and strengths $\sigma_u$ in Fig. 1(b-f), the discovery of compositions (iv) and (vi) resulted in the most ductile behavior; the largest products $\sigma_u\epsilon_u$ and $\sigma_u\epsilon_u\dot{\epsilon}$, as shown subsequently in Fig. 6(right). The most ductile composition was $Zr_{65}Cu_{40}Ni_7Al_{10}$ (iv): high products $\sigma_y\epsilon_y$, $\sigma_y\epsilon_y\dot{\epsilon}$, $\sigma_u\epsilon_u$, $\sigma_u\epsilon_u\dot{\epsilon}$, and also high stability of the test results (lowest deviation). Therefore, this composition was further investigated. A major question which still remains is which structural characteristics resulted in the material´s re-hardening (SB-diffusion and delocalization of the plastic flow) and superior ductility.

SEM fractographs and differential scanning calorimetry (DSC) results in Fig. 4 provided additional

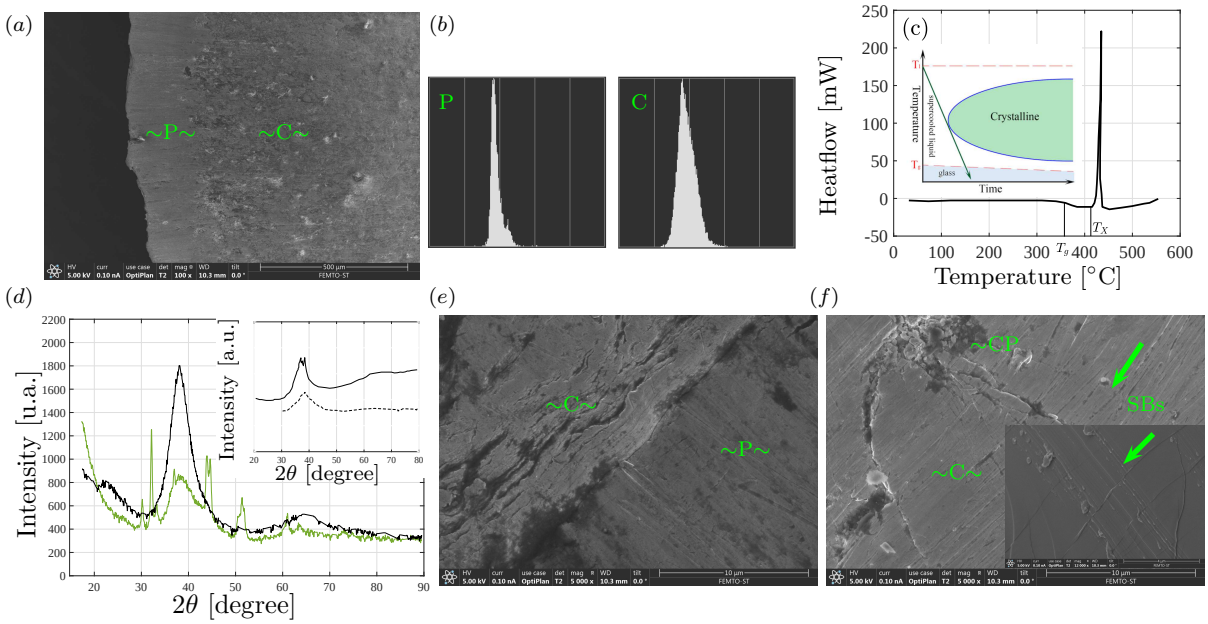


Figure 4: SEM image (top view) acquired before the monotonic compression test ($V = 0.1$ mm/s, RT, $Zr_{65}Cu_{15}Ni_{10}Al_{10}$) showing the outline between the periphery ∼P∼ and core ∼C∼ of the specimen (a). Normalized number of pixels (from zero to one) in the distribution (from zero to one) of the degree of darkness (from zero (black) to one (white)) in the P and C (b). The DSC curve with the heating rate of 3 K/min (the inset demonstrates a TTT diagram for the cooling rate for crystallization) (c). The XRD patterns (as-cast state) in the P (black) and the C (green) (d). The inset shows main characteristics of the XRD patterns (in arbitrary units) for the compositions (ii) (dashed) and (iii) (solid) extracted from [29] and [30], respectively. A detailed interface between the P and C (e). SBs and their slip planes (diagonal lines, highlighted by the green arrows) and the crossing microcracks (black) around a crystallized particle (CP, dark appearance) within C at the end of the test (f). The inset shows SBs and microcracks around the CP in more detail.

evidences for superior ductility. The degree of crystallization (DC), i.e., the portion of crystallized particles (dark spots or regions in Fig. 4(a)) was practically reduced to zero in the 'near-surface region' or the periphery (P) of the specimens during casting in cooled copper molds, implying the formation of supercooled liquid region [42]. However, the core (C) was metastable and partially crystallized to achieve thermodynamic equilibrium [32, 43]. The observed inhomogeneity of crystallization is a known characteristic of casting methods because of more rapid cooling of the P [44]. The corresponding histograms of the image analysis in Fig. 4(b) confirmed this; the standard deviation (SD) of the degree of darkness (DD) in the C (0.052) was 38 % greater than in the P, and the area of the peak used to estimate the increase in crystallization was approximately 25 % greater in the C. The DSC result in Fig. 4(c) shows that the super liquid region (SLR) defined by the difference of the crystallization and glass transition temperatures $T_X - T_g$ was rather limited, 45 °C. Moreover, the value of $T_X$ being far below the liquidus temperature $T_l$ (∼850 °C) achieved in the casting indicates that some crystallization formed; the cooling path pierced through the tip of the crystallized region in the time–temperature–transformation (TTT) diagram, Fig. 4(c). The XRD measurements in Fig. 4(d) confirmed this: a broad diffraction peak occurs in the P, whereas the diffraction remains low in the C, that is, a dispersed crystalline phase can be detected. The DC (the ratio of the areas of the crystalline peaks to the total area) in the C was observed to be approximately 5 %, and it constituted of homogeneously distributed nanocrystals and their heterogeneously distributed clusters or dendrites (crystallites) with varying shape. The size of the largest mesoscopic clusters ~~of homogeneously distributed crystallized mesoscopic particles or dendrites (crystallites) with varying shape~~ was around 1 $\mu$m, cf. Fig. 4(a,f). No sharp diffraction peaks indicating crystallization was observed in more brittle compositions (i) - (iii), see Fig. 4(d) and [24, 29, 30]. It was concluded that the meso-crystallites govern the phase presentation and microstructure of most ductile BMGs.

During casting, the contact surface between the C and P remained intact, although certain crystallization

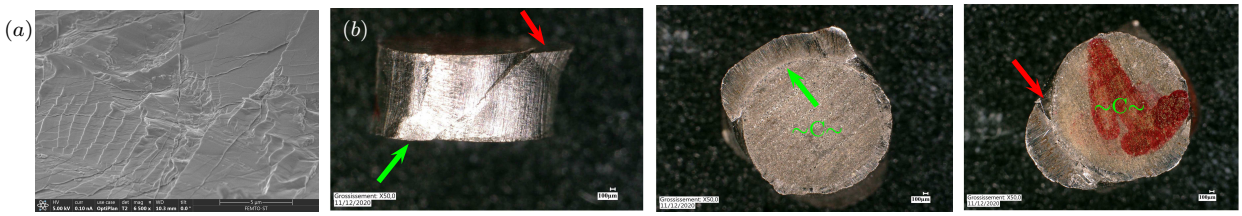


Figure 5: SEM image acquired from fracture surface towards the P after the monotonic compression test ($V = 0.1$ mm/s, RT, $Zr_{65}Cu_{15}Ni_{10}Al_{10}$) showing a network of short SBs and rippled zones (a). Visualization of the shape of the ruptured specimen (A2-1) (the side, bottom, and top views) using the Werth video-check machine (b).

was observed, cf. black shadings in Fig. 4(e). At the end of the monotonic test (re-hardening before rupture of the specimen), (a) short local microcracks extended but stopped at the crystallites, while the front of several crossing SBs stopped at said crystallites and local microcracks increasing ductility, Fig. 4(f). Accordingly, based on transmission electron microscopy (TEM) examinations [15], increased plastic flow (at low rates and temperatures) and ductility have been associated with the precipitation of nanocrystallites within the glass. The BMGs without said as-cast crystallites generally do not possess sufficient intrinsic micromechanisms to mitigate high stress concentrations at crack tips to produce extremely high ductility [15, 45]. For instance, the observed crystalline phase in composition (iv) explains its superior ductility over its glassy counterpart, which shows a restricted compressive strain less than 20 % [36] (without additional processing stages including plastic forming and heat treatment) being close to the limited values of compositions (i)-(iii). A comparison of Figs. 2(a) and 4(f) also revealed that the number of SBs (diffusion) increases and their thickness remains low with compressive deformation (a consecutive series of SBs sequentially accommodates increments of applied macroscopic strain [15]), and the SBs and their slip planes present during the first hardening were intersected by microcracks during the re-hardening. Therefore, microcracks initiated during softening (between the said two hardenings) showing a rapid stress drop [15]. Due to the occurrence of crystallites, under the compressive stress field, the microcracks and SBs cannot propagate freely, and a steady-state condition and a prolonged re-hardening could be observed. In addition, (b) rippled zones of SBs were located in fracture surfaces which were more far way from the second phase crystallites, further increasing ductility [15, 23, 38], Fig. 5(a). Therefore, the said two characteristics (a) - (b) for as-cast crystallization and chemical composition, were considered as the underlying micromechanisms of re-hardening and extreme plasticity at higher strain rates ($\dot{\epsilon} \sim 0.04$ 1/s); the super ductility was not a result from the high GFA, stress-induced nanocrystallization [22] or mere diffusion of SBs in tough and completely glassy metal [14, 27].

Finally, the specimens showed crack transection (highlighted by the arrows in Fig. 5(b)) and failure into flakes [30]. Collapse of the specimens was rapid and took place after the ultimate strain limit $\epsilon_u \sim 0.7$ shown in Fig. 1(b). The deformed shapes of the specimens showed failure surfaces which occurred at an angle of approximately 45° to the loading direction, referring to concentrated SBs and their expansion to microcracks affecting finally a sudden cracking and rupture of the specimens [17, 28, 29, 31, 35, 46]. Comparison of Figs. 4(a) and 5(b) reveals that the most significant failure surface occurred in the glassy periphery and between the P and C, whereas sufficiently crystallized core remained intact, i.e., sufficient crystallization improved ductility. As shown in Fig. 4(a), the thickness of P varies between 150 – 240 $\mu$m which is less than 8 % of the diameter of the sample. Therefore, ductility and plasticity could be significantly improved by grinding the P and only leave C.

## 3. Methods

**Prerequisites.** Low-cost and relatively ductile Zr-Cu-Ni-Al(-Ti) and Zr-Ti-Cu-Be compositions, which were discovered in the 90s were benefited in this study [17, 47]. However, development of highly ductile Zr-based compositions has been reported to be sensitive to chemical composition [10, 26, 27]. Al, Cu, Ni, and Be have lower melting points (725 °C, 1100 °C, 1455 °C, 1285 °C) than that of Zr (1850 °C), which low melting points are correlated with an improved GFA and a reduced $T_g$ of the final compositions; the lower the $T_g$ (and the higher the ratio $T/T_g$), the more ductile the composition near $T =$ RT [17, 18]. Furthermore, a low elastic modulus $E$ reflects a low $T_g$ and ductility[27]; therefore commonly used Zr ($E = 95$ GPa) and

Al ($E$ = 70 GPa) were selected as the components to form the BMG's major solvent [2]. Ti and Be have been found to increase ductility further, even with reduced Zr content [17, 47]. Moreover, the composition $Zr_{52.5}Cu_{17.9}Ni_{14.6}Al_{10}Ti_5$ has been reported to show extremely large strains of over 70 % [8] (AR ∼0.5, $\dot{\epsilon}$ ∼0.002 1/s) similar to $Zr_{65}Cu_{15}Ni_{10}Al_{10}$ [36], whereas $Zr_{57}Cu_{20}Ni_8Al_{10}Ti_5$ was considerably more brittle [24]. Therefore, remarkably ductility was achieved at Cu content of approximately 18 %, Ni content of between 10 and 15 %, and the Zr contents of between 52 and 65 % [25].

Moreover, formation of a sufficient DC in a bulk metallic matrix [26, 38, 44] as well as nanocrystallization in BMGs [16, 21, 22] during cooling have been shown to be an efficient way to increase ductility during loading. Therefore, a low DC (< 10 %) was enabled to be formed by limiting the cooling rate of the mold below 200 °C/s; when cooling down at a high enough cooling rate, such as 100...1000 °C/s depending on the composition, the crystallization is suppressed and perfect BMGs are produced [48, 49]. Observation of DC was based on three methods: 1) the difference of the degree of darkness, 2) DSC, and 3) XRD shown in Fig. 4. Electron Backscatter Diffraction (EBSD) as an advanced accurate method for determining DC [50] should be also mentioned for further research. From these basics, super ductile Zr-based compositions (at%) $Zr_{65}Cu_{15}Ni_{10}Al_{10}$ (iv), $Zr_{52.5}Cu_{17.8}Ni_{14.5}Al_{10}Ti_5$ (v), and $Zr_{40}Ti_{25}Cu_8Be_{27}$ (vi) were obtained and manufactured by a supplier from Xi'an, China. The $T_g$ values of these compositions were low, 360 °C [36], 400 °C [51], and approximately 330 °C [52], respectively. The ductility of compositions is compared in Fig. 6, showing the compositions (iv) and (vi) are the most ductile.

A difference in crystallization between the periphery and core of the specimens was observed due to more rapid cooling of the periphery (typical characteristic of the casting methods) [44]. The observed inhomogeneity of crystallization after casting was utilized, that is, amorphous periphery and slightly crystallized core (as-cast specimens) were compared and the influence of crystallization was investigated using one and the same specimen. In the investigated scenario, the homogeneously distributed crystallized nanoscopic particles or dendrites and their clusters (around 1 $\mu$m) with varying shape (within the core) were confirmed to consist mainly of CuZr because of its dark grey appearance in relation to the light glassy material [21] (Fig. 4(a,f)) and its highest melting point (1100 °C) in the ingot. A high Zr content is also known to increase crystallization in Zr-based BMG(C)s [22, 26, 29, 38]. The XRD results showed that a marked portion of the glassy material ∼35 % consists of Cu-Al including light Al up to 82 % and the Zr content of the crystallites is high (up to 99 %). The crystallites included oxygen, which is the most common atomic impurity in BMGs (in addition to hydrogen) reducing their glass-forming ability (GFA) because the impurities can easily move to fill up new, excessive free volume [17]. That is, in addition to low cooling rate affecting crystallization, the simple mixture law of the components of the ingot (especially the high Zr content relative to that of Cu) directly influenced ductility [27].

In addition to the compositions (iv) - (vi), the Zr-based compositions (at%) (i) $Zr_{57}Cu_{20}Ni_8Al_{10}Ti_5$ [24], (ii) $Zr_{48}Cu_{45}Al_7$ [29], and (iii) $Zr_{65}Cu_{18}Ni_7Al_{10}$ [30], taken from the literature, were compared. Specimens with compositions (i) and (iv) - (vi) (low Cu content) were manufactured by suction casting under similar conditions, and specimens with compositions (ii) and (iii) (low Ni/Al relationship) were manufactured by injection molding under equivalent conditions. The effects of the manufacturing method on the macroscopic deformation near RT were assumed to be small with regard to the chemical composition.

**Manufacturing and testing.** Metallic glasses (iv) - (vi) were elaborated in two successive steps. (i) First, a mother alloy (homogeneous ingot feedstock not in an amorphous state) was formed. For this purpose, constituent elements of very high purity (greater than 99.9 wt%) were mixed and subsequently melted by arc melting under the argon atmosphered vacuum. Four successive melts were performed to ensure an extremely high homogeneity. (ii) These master alloys were then remelted under vacuum and finally poured by suction casting into a water-cooled copper mold.

Approximately 50-mm-long cylindrical as-cast rods with a diameter of 3 mm were manufactured. High ductility has been reported to depend on AR [8, 22], and the rods were cut (using electrical discharge machining (EDM)) into 3-mm-long pieces to obtain a nominal aspect ratio (AR; height:diameter = 1:1) in accordance with the ASTM E9-89a (2000) standard for testing high-strength materials [22]. This low AR, in contrast to 1.6:1 or higher [17, 22, 24, 29, 31], enabled the observation of higher ductility without premature buckling and failure of the specimens into flakes during compression tests. The scanning electron microscope (SEM) imaging (FEI Quanta 450 W EDS EDAX), X-ray diffraction (XRD) (Bruker D8 Discover diffractometer equipped with an Atlas goniometer), differential scanning calorimetry (DSC) (SETARAM DSC 131 Evo, 3 °C/min over a temperature range of 30 °C to 550 °C in the high purity dry nitrogen

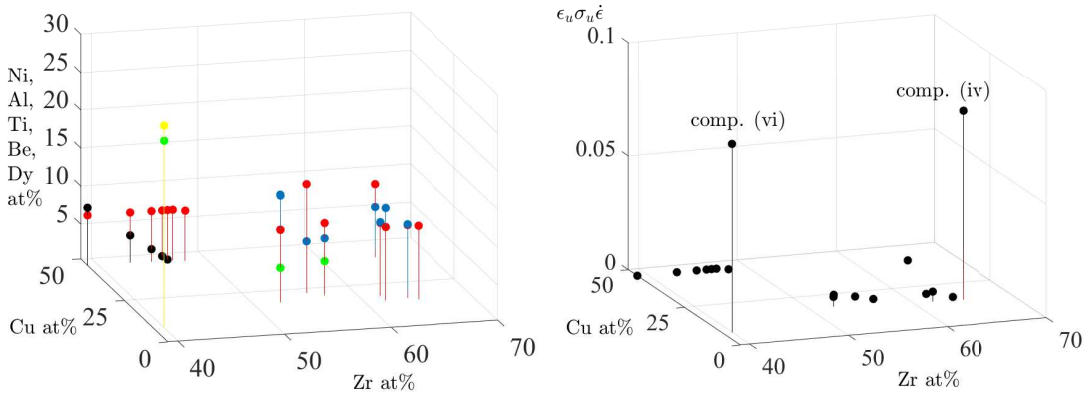


Figure 6: Ductile compositions[11, 24, 27, 29–31] (Ni, Al, Ti, Be, Dy are highlighted by the blue, red, green, yellow, and black) (left), and their ductility in terms of the product of the ultimate strength, strain, and strain rate, $\sigma_u\epsilon_u\dot{\epsilon}$ (right).

atmosphere), and image analysis of the test specimens (cutted from the as-cast rods) were performed to ascertain their amorphous nature.

Because BMGs are brittle in tension [4, 15], compression tests were a consistent choice, and the results also benefit the ductility for tension. No specific standards exist for testing large deformations in BMGs. It is known that low loading rate increases deformability [22]. The following uniaxial tests under compression were performed using an MTS Criterion 45 machine equipped with a 100 kN load cell: monotonic, quasi-static displacement-controlled tests at RT and deformation rates of $V = 0.01$, 0.1, and 1 mm/s ($\dot{\epsilon} = 0.003 - 0.33$ 1/s) until sample rupture; corresponding tests at $V = 0.01$ mm/s and at temperatures of 160 °C and 300 °C were also performed. The deformed shapes of the specimens were analyzed by the non-contact metrology by the Werth video-check machine and the cross-sectional surfaces were imaged by SEM. The test sets were designed to monitor the yield strength and strain, hardening-softening behavior (stress drop) at RT, and the maximum strain rate for re-hardening and ultimate strains ($\epsilon_u > 0.6$).

To ensure exact alignment of the specimens, the machine platens were placed next to each other and adjusted prior to the tests, which tests were controlled in terms of the speed of movement of the top platen, $V$, and the axial force, $F$. The corresponding axial strain rate was $\dot{\epsilon} = V/H$, where $H$ is the initial height of the specimen. The engineering strain is $\epsilon = \Delta H/H$, where $\Delta H = h - H$ and $h$ is the final height. The (machine) stress was calculated as $\sigma = F/A$, where $A$ is the initial cross-sectional area of the specimen. The negative sign for compression (stress and strain) was omitted from the results for simplicity. This 1st Piola-Kirchhoff stress and the engineering strain were easy to measure [8, 53]. For comparison, the true stress ($F$ divided by the current area, which area was recorded by the Werth video-check machine) vs. $\epsilon$ is shown in Fig. 1(c). Despite the difference between the stress measures during extreme strains, the high ductility including re-hardening was a distinct material characteristic of the compositions (iv) - (vi) applied.

## 4. Conclusion

The extreme plastic deformability (ductility) strongly depended on chemical composition (from RT to 300°C); the highest ductility was achieved by the low Cu content (8 - 18 at%) with sufficient contents of Zr, Ti, or Be (52 - 65, 5 - 25, and ∼27 at%, respectively), and low contents of Ni and Al (0 - 15 at% depending on the Be content). The lower the strain rate $\dot{\epsilon}$, the lower the yield strength ratio $\sigma^y/\sigma^c$ and the higher the ductility. A sufficient amount (DC∼5 %) of nanoscopic crystallized particles and their clusters (up to 1 $\mu$m) consisting mainly of Zr significantly increased ductility because the crystallites efficiently hindered the extension of SBs and microcracks within glassy regions. The most ductile BMGs $Zr_{65}Cu_{15}Ni_{10}Al_{10}$ and $Zr_{40}Ti_{25}Cu_8Be_{27}$ showed hardening and extreme deformability of 70 % yet at strain rates of almost $\dot{\epsilon} = 0.04$ 1/s at RT. Compared to previous state-of-the-art results, ductility, in terms of the product $\sigma_u\epsilon_u\dot{\epsilon}$, was increased over 1,500 %. We have now a concrete solution for developing extremely ductile BMGs near RT: optimal chemical composition (at%) and DC. It would be interesting in future to investigate the deformation characteristics of the most ductile BMGs also under other loading conditions. Extreme ductility and plasticity could further be

improved by grinding the periphery (P) and only leave the core (C). Alternatively, manufacturing could be optimized relative to the thickness of the P. Moreover, detailed effects of frequency and size of the crystallites (in connection with SBs) on superior ductility (e.g., by TEM) is an interesting research object in future.


### Acknowledgements

The research was supported by the EIPHI Graduate School (contract ANR-17-EURE-0002) including its experimental facilities (cutting of test specimens, Werth video-check, X-ray tomography, SEM, and optical 3D metrology). The authors are grateful to MIFHySTO technological platform for the use of equipments and to J.C QIAO (NWPU, Xi'an, China) for providing the materials. We also thank Flora Regad-Pelagru for the SEM figures.


### Contribution of authors

All authors contributed the literature review. S.H., T.B., and X.G designed the experiments. J.M.P. provided the material, and T.B. arranged the testing facilities. X.G and S.C conducted the mechanical tests on different materials, and N.N performed the Werth video-check and DSC measurements. S.H. wrote the majority of the paper. J.M.P. and W-H.W analyzed the results. T.B., J.M.P., and W-H.W participated in the writing of the paper. F.B. conducted and analyzed the XRD-tests.

### Competing interests

The authors declare no competing interests.

### Data availability

All relevant data (at different temperatures RT, 160°C, and 300°C) are available from the corresponding authors upon reasonable request.

## References


[1] K. Zhao, X. X. Xia, H. Y. Bai, D. Q. Zhao, and W. H. Wang. Room temperature homogeneous flow in a bulk metallic glass with low glass transition temperature. *Appl. Phys. Lett.*, 98:141913, 2011.

[2] C. Suryanarayana. Mechanical behavior of emerging materials. *Mater. Today*, 15:486–498, 2012.

[3] X. Mu, M. R. Chellali, E. Boltynjuk, D. Gunderov, R. Z. Valiev, H. Hahn, C. Kübel, Y. Ivanisenko, and L. Velasco. Unveiling the local atomic arrangements in the shear band regions of metallic glass. *Adv. Mater.*, 33:2007267, 2021.

[4] Z. Lu and et al. Substantially enhanced plasticity of bulk metallic glasses by densifying local atomic packing. *Nat. Commun.*, 12:6582, 2021.

[5] J. C. Qiao and J. M. Pelletier. Dynamic mechanical relaxation in bulk metallic glasses: A review. *J. Mater. Sci. Technol.*, 30:523–545, 2014.

[6] J. Han, U. Jeong, Y. Lee, K. P. Marimuthu, and H. Lee. Determination of parameters of free volume model for Zr-based BMG via nanoindentation. *Intermetallics*, 131:107121, 2021.

[7] K. Pulidindi and S. Mukherjee. Metallic glass market size 2020 - 2026. report ID: GMI4722. Technical report, Global Market Insights, 2020.

[8] H. Bei, S. Xie, and E. P. George. Softening caused by profuse shear banding in a bulk metallic glass. *Phys. Rev. Lett.*, 96:105503, 2006.

[9] L. Zhao, D. Han, S. Guan, X. Lu, K. Chan, and G. Wang. Simultaneous improvement of plasticity and strength of metallic glasses by tailoring residual stress: Role of stress gradient on shear banding. *Mater. Des.*, 197:109246, 2021.

[10] Y. Wu, Y. Xiao, G. Chen, C.T. Liu, and Z. Lu. Bulk metallic glass composites with transformation-mediated work-hardening and ductility. *Adv. Mater.*, 22:2770–73, 2010.

[11] J. C. Qiao, Y. Yao, J. M. Pelletier, and L. M. Keer. Understanding of micro-alloying on plasticity in $Cu_{46}Zr_{47-x}Al_7Dy_x$ ($0 \leq x \leq 8$) bulk metallic glasses under compression: Based on mechanical relaxations and theoretical analysis. *Int. J. Plast.*, 82:62–75, 2016.

[12] J. Pan, Y. P. Ivanov, W. H. Zhou, Y. Li, and A. L. Greer. Strain-hardening and suppression of shear- banding in rejuvenated bulk metallic glass. *Nature*, 578:559–562, 2020.

[13] E. D. Cubuk, R. J. S. Ivancic, S. S. Schoenholz, and D. J. Strickland. Structure-property relationships from universal signatures of plasticity in disordered solids. *Science*, 358:1033–1037, 2017.

[14] E. Ma. Controlling plastic instability. *Nat. Mater.*, 2:7–8, 2003.

[15] C. A. Schuh, T. C. Hufnagel, and U. Ramamurty. Mechanical behavior of amorphous alloys. *Acta Materialia*, 144:4067–4109, 2007.

[16] B. S. Li, S. Xie, and J. J. Kruzic. Toughness enhancement and heterogeneous softening of a cryogenically cycled Zr-Cu-Ni-Al-Nb bulk metallic glass. *Acta Materialia*, 176:278–288, 2019.

[17] J. J. Kruzic. Bulk Metallic Glasses as Structural Materials: A Review. *Adv. Eng. Mater.*, 18:1308–1331, 2016.

[18] C. Wang, Q. P. Cao, X. D. Wang, D. X. Zhang, U. Ramamurty, R. L. Narayan, and J-Z. Jiang. Intermediate temperature brittleness in metallic glasses. *Adv. Mater.*, 29:1605537, 2017.

[19] Y. Du, W. Han, Q. Zhou, Y. Xu, H. Zhai, V. Bhardwaj, and H. Wang. Enhancing the plasticity of a Ti-based bulk metallic glass composite by cryogenic cycling treatments. *J. Alloys Compd.*, 835:155247, 2020.

[20] X. Yuan, D. Sopu, F. Spieckermann, K. K. Song, S. V. Ketov, K. G. Prashanth, and J. Eckert. Maximizing the degree of rejuvenation in metallic glasses. *Scr. Mater*, 212:114575, 2022.

[21] T. Wang, Y. Wu, J. Si, Y. Liu, and X. Hui. Plasticizing and work hardening in phase separated Cu-Zr-Al-Nb bulk metallic glasses by deformation induced nanocrystallization. *Mater. Des.*, 142:74–82, 2018.

[22] F. Qiu, P. Shen, T. Liu, and Q. Jiang. Enhanced ductility in a $Zr_{65}Cu_{15}Al_{10}Ni_{10}$ bulk metallic glass by nanocrystallization during compression. *Mater. Des*, 36:168–171, 2012.

[23] L. S. Luo, B. B. Wang, F. Y. Dong, Y. Q. Su, E. Y. Guo, Y. J. Xu, M. Y. Wang, L. Wang, J. X. Yu, R. O. Ritchie, J. J. Guo, and H. Z. Fu. Structural origins for the generation of strength, ductility and toughness in bulk-metallic glasses using hydrogen microalloying. *Acta Materialia*, 171:216–230, 2019.

[24] J.J. Fan, Y.F Yan, S.H. Chen, C-H Ng, F.F Wu, and K.C Chan. Reliability of the plastic deformation behavior of a Zr-based bulk metallic glass. *Intermetallics*, 74:25–30, 2016.

[25] X. Du, J. C. Huang, K-C. Hsieh, J. S. C. Jang, P. K. Liaw, H-M. Chen, H-S. Chou, and Y-H. Laig. Designing ductile zr-based bulk metallic glasses with phase separated microstructure. *Adv Eng Mater*, 11:387–391, 2009.

[26] L. Krämer, Y. Champion, and R. Pippan. From powders to bulk metallic glass composites. *Nature Scientific Reports*, 7:6651–59, 2017.

[27] Y. H. Liu, G. Wang, R. J. Wang, D. Q. Zhao, M. X. Pan, and W. H. Wang. Super plastic bulk metallic glasses at room temperature in disordered solids. *Science*, 315:1385–1388, 2007.

[28] H. S. Shahabi, S. Scudino, I. Kaban, M. Stoica, U. Rütt, U. Kühn, and J. Eckert. Structural aspects of elasto-plastic deformation of a Zr-based bulk metallic glass under uniaxial compression. *Acta Materialia*, 95:30–36, 2015.

[29] W. F. Wu, Y. Li, and C. A. Schuh. Strength, plasticity and brittleness of bulk metallic glasses under compression: statistical and geometric effects. *Philos. Mag.*, 1:71–89, 2008.

[30] D. Zhou, B. Hou, B. Li, S. Zhang, L. Dai, and Y. Li. A comparative study of the rate effect on deformation mode in ductile and brittle bulk metallic glasses. *Intermetallics*, 96:94–103, 2018.

[31] K. Zhu, P. Tao, C. Zhang, Z. Zhao, W. Zhang, Y. Yang, and K. Kaviyarasu. Effect of strain rates on the plastic deformation behavior and serrated flow of $Zr_{55.7}Cu_{22.4}Ni_{7.2}Al_{14.7}$ bulk metallic glass. *Mater. Today Commun.*, 27:102320, 2021.

[32] X. Tong, G. Wang, Z. H. Stachurski, J. Bednarčík, N. Mattern, Q. J. Zhai, and J. Eckert. Structural evolution and strength change of a metallic glass at different temperatures. *Nature Sci. Rep.*, 6:30876, 2016.

[33] J. Zhang, H. Jiang, C. Jiang, G. Kang, and F. Lu. Stochastic deformation and shear transformation zones of the glassy matrix in CuZr-based metallic-glass composites. *Int. J. Plast.*, 125:52–62, 2020.

[34] Y. P. Jiang, X. P. Shi, and K. Qiu. Numerical study of shear banding evolution in bulk metallic glass composites. *Mater. Des.*, 77:32–40, 2015.

[35] L. Anand and C. Su. A theory for amorphous viscoplastic materials undergoing finite deformations, with application to metallic glasses. *J. Mech. Phys. Solids*, 53:1362–1396, 2005.

[36] G. V. Afonina, Yu. P. Mitrofanova, N. P. Kobelevb, and V. A. Khonik. Shear modulus relaxation and thermal effects in a $Zr_{65}Cu_{15}Ni_{10}Al_{10}$ metallic glass after inhomogeneous plastic deformation. *J. Exp. Theor. Phys.*, 131:582–588, 2020.

[37] J. Brechtl, X. Xie, Z. Wang, J. W. Qiao, and P. K. Liaw. Complexity analysis of serrated flows in a bulk metallic glass under constrained and unconstrained condistions. *Mater. Sci. Eng. A*, 771:138585, 2020.

[38] S. Cardinal, J. M. Pelletier, G. Q. Xie, and F. Mercier. Manufacturing of cu-based metallic glasses matrix composites by spark plasma sintering. *Mater. Sci. Eng. A*, 711:405–414, 2018.

[39] T. Barriere, X. Gabrion, and S. Holopainen. A compact constitutive model to describe the viscoelastic-plastic behaviour of glassy polymers: Comparison with monotonic and cyclic experiments and state-of-the-art models. *Int. J. Plast.*, 122:31–48, 2019.

[40] T. Barriere, X. Gabrion, S. Holopainen, and J. Jokinen. Testing and analysis of solid polymers under large monotonic and long-term cyclic deformation. *Int. J. Plast.*, 135:102781, 2020.

[41] E. S. Park. Understanding of the shear bands in amorphous metals. *Applied Microscopy*, 45:63–73, 2015.

[42] N. Sohrabi, J. Jhabvala, and R. E. Logá. Additive manufacturing of bulk metallic glasses-process, challenges and properties: A review. *Metals*, 11:1279, 2021.

[43] A. Gulzar, L. Z. Zhao, R. J. Xue, K. Shahzad, D. Q. Zhao, and W. H. Wang. Correlation between flow units and crystallization in metallic glasses. *J Non Cryst Solids*, 461:61–66, 2017.

[44] X. Fu, G. Wang, Y. Wu, W. Song, C. H. Shek, Y. Zhang, J. Shen, and R. O. Ritchie. Compressive ductility and fracture resistance in CuZr-based shape-memory metallic-glass composites. *Int. J. Plast.*, 128:102687, 2020.

[45] K. M. Flores and R. H. Dauskardt. Enhanced toughness due to stable crack tip damage zones in bulk metallic glass. *Scripta Materialia*, 41:937–943, 1999.

[46] J Zhou, Q. Wang, Q. Zeng, K. Yin, A. Wang, J. Luand, L. Sun, and B. Shen. A plastic FeNi-based bulk metallic glass and its deformatin behavior. *J. Mater. Sci. Technol.*, 76:20–32, 2021.

[47] D. C. Hofmann. Bulk metallic glasses and their composites: A brief history of diverging fields. *J. Mater.*, 2013.

[48] D. Singh, R. K. Mandal, R. S. Tiwari, and O. N. Srivastava. *Mechanical Behavior of Zr-Based Metallic Glasses and Their Nanocomposites. In: Movahedi, B. (Ed.), Metallic Glasses - Formation and Properties.* IntechOpen, 2016.

[49] W. Yin. *Compressive behavior of bulk metallic glass under different conditions - coupled effect of temperature and strain rate. PhD thesis.* The University of North Carolina, The United States, 2013.

[50] W. Wisniewski, P. Švančárek, A. Prnová, M. Parchovianský, and D. Galusek. $Y_2O_3$-$Al_2O_3$ microsphere crystallization analyzed by electron backscatter diffraction (EBSD). *Nature Sci. Rep.*, 10:11122, 2020.

[51] R. F. Tournier. Glass phase and other multiple liquid-to-liquid transitions resulting from two-liquid phase competition. *Chem. Phys. Lett*, 665:64–70, 2016.

[52] H. Zong, L. Bian, J. Cheng, G. Cao, C. Kang, and Ming Li. Glass forming ability, thermal stability and elastic properties of Zr-Ti-Cu-Be-(Fe) bulk metallic glasses. *Results Phys.*, 6:1157–1160, 2016.

[53] T. Barriere, A. Cherouat, X. Gabrion, and S. Holopainen. Short- to long-term deformation behavior, failure, and service life of amorphous polymers under cyclic torsional and multiaxial loadings. *Int. J. Plast.*, 147:103106, 2021.